Article citation info:
Shen J, Liu Y, Zheng Y. Axlebox bearing fault diagnosis method for rolling stock combining improved CEEMD and MOMEDA. Diagnostyka. 2024;25(4):2024402. https://doi.org/10.29354/diag/192497.

DIAGNOSTYKA, 2024, Vol. 25, No. 4

e-ISSN 2449-5220
DOI: 10.29354/diag/192497

AXLEBOX BEARING FAULT DIAGNOSIS METHOD FOR ROLLING STOCK COMBINING IMPROVED CEEMD AND MOMEDA

Jiuli SHEN [1, *], Yiako LIU [1], Yan ZHENG [2]

[1] Huzhou Vocational and Technical College, Huzhou, 313099, China
[2] The Intelligent Manufacturing and Maintenance Application Technology Research and Development Center for University High-speed Train Units in Hebei Province, Tangshan Polytechnic University, Tangshan, 063299, China

[*] Corresponding author, e-mail: sjlysu2016@sina.com

Abstract

To enhance the effectiveness of diagnosing axial bearing fault signals in moving trains, this study proposes a method that combines improved complementary set empirical modal decomposition and optimal minimum entropy deconvolutional adjustment. There are plans to develop a screening method based on intrinsic modal function components to further boost the diagnostic procedure's effectiveness. The simulation experimental validation showed that the fault eigenfrequencies from 1 to 7 octave may be identified by the research-proposed method after envelope spectral analysis. Case Western Reserve University dataset validation indicated that the proposed method is superior in terms of bearing fault signal processing results. The time-domain amplitude of the inner ring fault signal increased by 50% and was increased at all times compared to other methods. The eigen frequency of the inner ring fault signal was found to be between 1 and 9 octaves, whereas the outer ring fault signal was found to be between 1 and 14 octaves. The findings show that the suggested approach is capable of accurately diagnosing axlebox bearing fault signals in the locomotive group and of directly localizing the fault location based on the envelope spectrogram's characteristic frequency.

Keywords: bearing fault detection; empirical modal decomposition; deconvolution; signal eigen frequency; vibration monitoring

1. INTRODUCTION

With the increasing scale of China's high-speed railroads, people are more and more concerned about the safety and reliability of the structural components of the rolling stock. Axlebox bearings (ABBs), as one of the main components that make up the bogie of a rolling stock, are able to convert the rotation of the bogie wheels into the straight-line motion of the train along the track, and also carry the overall weight of the entire rolling stock [1-3]. However, the high-speed operation of rolling stock is accompanied by corresponding wear and consumption, which can easily lead to corrosion, corrosion and cracks in rolling bodies, inner rings, outer rings and cages, thus aggravating the phenomena of burnt shafts, seized wheelsets and operation noise, and even leading to safety accidents in rolling stock. Therefore, it is very important to carry out timely and effective fault diagnosis and monitoring (Fault Diagnosis, FD) of the ABB of the rolling stock. In the normal operation of the axlebox of the locomotive set, timely detection and diagnosis of the early weak faults can effectively avoid the occurrence of bearing failures. The current fault detection methods for ABB are mainly temperature, sound and vibration monitoring (VM). However, in VM, the interference of vibration signal (VS) identification increases due to the addition of electromagnetic excitations and loads to simulate the train operation in the ABB test bed of the rolling stock during the experimental process [4-5]. Furthermore, the vibration sensor positioned at the end cap will be impacted during the signal collection process, making signal processing in the ABB FD process very important [6]. Based on this, a fault diagnosis method for high-speed train axle box bearings is proposed from the perspective of vibration signal denoising. First, the original signals of the monitored vibration data were decomposed into Intrinsic Mode Function (IMF) components using Complementary Ensemble Empirical Mode Decomposition (CEEMD). Secondly, the IMF components are selected according to the comprehensive indicators such as Kurtosis (K), Fault Impact Ratio (FIR) and Pearson Coefficient of Correlation (PCC) to obtain the Reconstructed Signal (Reconstructed Signal (RS). Finally,

Received 2024-03-21; Accepted 2024-08-21; Available online 2024-09-23

Multipoint Optimal Minimum Entropy Deconvolution Adjusted (MOMEDA) is utilized to deconvolution calculation and envelope analysis of RS, so as to diagnose the faulty parts of axle box bearings.

The study's overarching framework is divided into four sections: in the first part, the research results and shortcomings of domestic and international research on bearing FD and VS analysis methods are summarized. In the second part, the FD method of ABB of moving train combined with improved CEEMD and MOMEDA is studied and designed. In the third part, the proposed FD method for moving train ABB is experimented and analyzed. In the fourth part, the experimental results are summarized and future research directions are indicated.

2. RELATED WORKS

Remote diagnosis is gradually being achieved by bearing fault detection (BFD) as a result of the advancement of Internet of Things technology. By installing sensors on the equipment, the operating data of the bearings are collected and transmitted to the remote diagnosis center through the Internet. Researchers both domestically and overseas have studied a variety of data-driven based diagnosis techniques. Aviña et al. investigated three types of fitted goodness-of-fit detection for the phenomenon of efficiency loss of induction motors under non-optimal operation, thus finding that induction motors have the most serious damage effects in single-point damage and distributed damage [7]. The safe operation of spinning machinery is directly influenced by the condition of the bearings. By using the period segment matrix as the trajectory matrix enabled the reconstruction of the signal without the need to select singular values, thus realizing the suppression of noise between adjacent fault pulses in the detection of fault pulses [8]. Habbouche et al. proposed an approach to early diagnosis of bearing failures based on variational modal decomposition and machine learning techniques [9]. This approach aims to reduce the cost of rolling bearing maintenance and ensure effective monitoring of bearing degradation. Zhou et al. proved a method that uses an asymmetric Gaussian chirp model to solve the coefficient representation table optimized to originate from the parameters using an orthogonal matching pursuit algorithm optimized by the pathfinder algorithm, thus achieving the best approximation of the original signal (OS) [10].

VS analysis technique is an important method used to study the vibration characteristics of mechanical equipment, and the current research on this method at home and abroad has achieved various results. Hosseinpour et al. presented a diagnostic approach that uses feature selection of correlation to identify the best characteristics and uses random forests and multilayer perceptron neural networks for classification in order to address the issue of the low efficiency of applying intelligent FD in tractors. The feasibility of this method in tractor auxiliary transmission FD was confirmed by performance validation in a dataset thus [11]. Wang et al. proposed a novel convolutional neural network model to address the problem that current methods can only use a single-dimensional signal. By utilizing wavelet variations and the short-time Fourier transform, the model was able to handle the original time-domain signals simultaneously and produce an effective output for a three-dimensional task [12]. Zhang created a simulation system model for directional current protection in MATLAB software. Zhang's model enabled him to ascertain that, even after signal gathering and processing, faults can be successfully discharged in scenarios such as two-phase grounded short circuits and two-phase packet circuits [13].

To sum up, researchers both domestically and internationally have conducted a variety of studies on bearing FD and signal analysis methodologies. Nevertheless, most of these research have concentrated on minor BFD and have had inadequate processing influence on other problems such as signal noise. Therefore, the study proposes a FD method for rolling stock ABB that combines the improved CEEMD and MOMEDA. Firstly, CEEMD is utilized for fault signal (FS) decomposition, then MOMEDA is utilized for deconvolution, and finally, envelope analysis is utilized for FD. Meanwhile, the study innovatively designs an IMF component screening method, which performs IMF component screening by indicators such as K, FIR, and PCC with a view to improving the efficiency of FD.

3. DESIGN OF A FAULT DIAGNOSIS METHOD FOR AXLEBOX BEARINGS IN ROLLING STOCK COMBINING IMPROVED CEEMD AND MOMEDA

To eliminate the interference or noise effects generated by the external environment of the rolling stock ABB test bed in VM and the simulation method, etc., the study proposes a FD method for the ABB that combines the improved CEEMD and MOMEDA. Firstly, the improved CEEMD method is introduced. Finally, the FD method design is carried out based on the improved CEEMD and MOMEDA.

3.1. Improved CEEMD methods

Empirical mode decomposition (EMD) was improved upon to create CEEMD, a decomposition technique. Without requiring the basis function to be predetermined, EMD can decompose the signal in accordance with the time scale features of the data itself [14-15]. It has a certain adaptive ability to the signal, and all signals can be decomposed into the sum of multiple empirical mode component (EMC) by EMD. Its main decomposition process is shown in Fig. 1.

m_1	Once the decomposed signal has been acquired, locate the local maximum and minimum extremum points. Next, fit the maximum and minimum points in the envelope using the spline curve fitting method. Finally, calculate the average m_1 of the upper and lower envelope.
h_1	If h_1 is an empirical mode component, then h_1 is the first IMF component of $x(t)$: If h_1 is not an empirical mode component, then h_1 is used as the original signal to repeat the previous step k times, and the calculation can be obtained after the iteration is completed.
r_1	Subtract c_1 from $x(t)$ to get the residual expression r_1
c_2	Repeat steps 1 through 4 with the resulting residual r_1 as the original signal to get the next component of $x(t)$, c_2.

Fig. 1. EMD signal decomposition process

Using the decomposed signals, the local maximum and minimum extreme points are first searched. IMF component identification is performed by determining whether the obtained value is the empirical modal component EMC.The process of finding the maximum and minimum extreme points is continued until the first IMF component is found if the value found is not the EMC. To find the residual, subtract the first IMF component from the signal. Repeating steps 1 through 4 with the residual as the OS yields the second IMF component. By repeating the calculation, multiple IMF components can be obtained. Obviously, the signal decomposition step of EMD may lead to modal aliasing during processing. Thus, the proposal is for ensemble empirical mode decomposition (EEMD). After multiplexed averaging based on the specificity of the mean-zero noise, EEMD adds Gaussian white noise (GWN) to the OS as an additional analysis. This causes the noises to inhibit each other. Therefore, the final IMF component expression formula of EEMD is shown in Equation (1).

$$w_n(t) = \frac{1}{n}\sum_{i=1}^{N} W_{in}(t) \tag{1}$$

In Equation (1), $w_n(t)$ denotes the final IMF component and $W_{in}(t)$ denotes the ensemble of IMF components at each stage. n is the stage of the IMF component and N is the ensemble of all stages of the decomposition. Nevertheless, the amplitude and energy of the OS are altered by the addition of white noise, which reduces the efficiency of the signal's decomposition. Therefore, C

EEMD is proposed to effectively compensate for the shortcomings of EEMD. CEEMD performs EMD by adding a set of white noise of the same size but opposite direction to EMD, and integrally averages the decomposition results [16-17]. Its main decomposition process is shown in Fig. 2.

The expression equation in Fig. 2 after a set of white noise is added to the OS is equation (2).

$$\begin{cases} x_1^+(t) = x(t) + m_1^+(t) \\ x_1^-(t) = x(t) + m_1^-(t) \end{cases} \tag{2}$$

In Equation (2), $x_1^+(t)$ and $x_1^-(t)$ denote the OS with forward and reverse GWN signals added, respectively, and $x(t)$ denotes the OS. $m_1^+(t)$ and $m_1^-(t)$ denote the forward and reverse GWN,

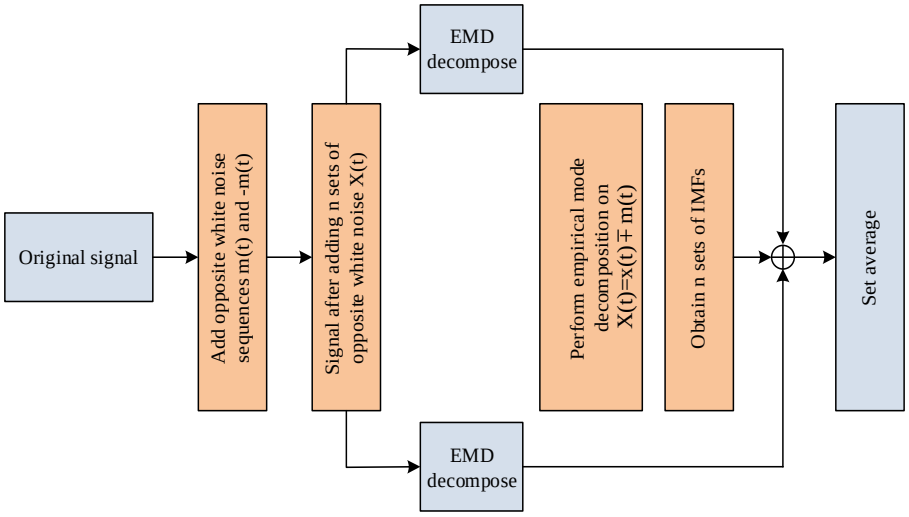

Fig. 2. CEEMD decomposition process

respectively, which are equal in size. Equation (3) illustrates the created IMF component expression of the signal, which is derived from the signal's calculated EMD decomposition after the white noise signal is added.

$$\begin{cases} x_i^+ = \sum_{j=1}^{n} w_{ij}^+(t) \\ x_i^- = \sum_{j=1}^{n} w_{ij}^-(t) \end{cases} \tag{3}$$

In Equation (3), x_i^+ and x_i^- denote the signals decomposed by EMD from the OS with forward and reverse GWN added, respectively. The IMF components that were acquired by decomposing the OS and adding forward and inverse GWN, respectively, are indicated by the letters $w_{ij}^+(t)$ and $w_{ij}^-(t)$. Based on the obtained IMF components. They are further aggregated to calculate their positive and negative averages to obtain the final IMF components, which are expressed as shown in Equation (4).

$$w_i(t) = \frac{1}{2n}\sum_{j=1}^{n}(w_{ij}^+(t) + w_{ij}^-(t)) \tag{4}$$

The CEEMD decomposition method can automatically generate the basis functions and sequentially generate the IMF components of each stage with unequal bandwidths according to the order of high and low. In the complex train operation reality, the faulty VS of the moving train set ABB belongs to the fluctuating and nonlinear signals, and the high-pass filtering characteristic of CEEMD is just enough to decompose it.

3.2. Enhanced bearing defect diagnostic technique integrating MOMEDA and CEEMD

It is examined to use MOMEDA to deconvolve the RS after noise reduction, and then incorporate the analysis, in accordance with the improved CEEMD for decomposition and noise reduction of ABB's VS. MOMEDA is an enhancement over minimum entropy deconvolution (MED), which is resolved using the D-parameter deconvolution concept. The best deconvolution solution is determined by the multi-D-Norm (MDN) as the objective function [18-19]. Equation (5) is thought to represent the OS expression function that MOMEDA in the sensor collected.

$$x(a) = h(a) \times k(n) + s(n) \tag{5}$$

In Equation (5), $x(a)$ denotes the OS obtained in the sensor and $h(a)$ denotes the response of the shock signal. $k(a)$ denotes the actual shock signal and $s(a)$ denotes the running noise signal. The expression equation for the recovery of the shock signal by MOMEDA through the optimal filter is shown in Equation (6).

$$k(a) = f(a) \cdot x(a) = \sum_{a=1}^{A-L} f_a x_{a+L-1} \tag{6}$$

In Equation (6), denotes the filter length and denotes the optimal filter in the sensor. denotes the optimal filter and denotes the signal length. Since there are multiple pulses in ABB's fault detection in its VS, the D-paradigm expression for MOMEDA is obtained by maximum value optimization on the basis of MDN, as shown in Equation (7).

$$MOMEDA: \max_{\vec{f}} MDN(\vec{\boldsymbol{y}}, \vec{\boldsymbol{t}}) = \max_{\vec{f}} \frac{\vec{\boldsymbol{t}}^{\mathrm{T}}\vec{\boldsymbol{y}}}{\|\vec{\boldsymbol{y}}\|} \tag{7}$$

In Equation (7), $\vec{\boldsymbol{y}}$ denotes the solution of the deconvolution and T is the transpose matrix. $\vec{f}$ is the optimal filter, and $\vec{\boldsymbol{t}}$ is the weight and position of the target pulse to be convolved. MOMEDA realizes the detection of bearing faults by deconvolution of the three pulses of the output signal, and prompts the deconvolution pulse to match the polarity of the signal by removing the absolute value. Therefore, the coefficient value of the filter can be obtained by the derivation of the D-parameter of MOMEDA, which is calculated as shown in Equation (8).

$$\frac{d}{df}\left(\frac{\vec{\boldsymbol{t}}^T\vec{\boldsymbol{y}}}{\|\vec{\boldsymbol{y}}\|}\right) = \|\vec{\boldsymbol{y}}\|(t_1\vec{\boldsymbol{M}}_1 + t_2\vec{\boldsymbol{M}}_2 + \cdots + t_{A-L}\vec{\boldsymbol{M}}_{A-L}) - \|\vec{\boldsymbol{y}}\|^{-3}\vec{\boldsymbol{t}}^T\vec{\boldsymbol{y}}X_0\vec{\boldsymbol{y}} \tag{8}$$

In Equation (9), $\vec{\boldsymbol{M}}$ denotes the set of filtered signals and X_0 denotes the initial RS. When the derivative of Equation (8) is 0, the expression is updated as shown in Equation (9).

$$\frac{\vec{\boldsymbol{t}}^T\vec{\boldsymbol{y}}}{\|\vec{\boldsymbol{y}}\|} X_0\vec{\boldsymbol{y}} = X_0\vec{\boldsymbol{t}} \tag{9}$$

Since MOMEDA needs to adjust its definition in ABB's FD, it is not suitable for input data without null hypothesis when only the output range is considered. And the multiplicity of filter coefficients still belongs to a solution of MOMEDA, so its optimal filter output formula is shown in Equation (10).

$$\vec{\boldsymbol{f}} = (\boldsymbol{X}_0\boldsymbol{X}_0^T)\boldsymbol{X}_0\vec{\boldsymbol{t}} \tag{10}$$

In Equation (10), $\vec{\boldsymbol{f}}$ denotes the optimal filter as well as the output solution, and $\boldsymbol{X}_0\boldsymbol{X}_0^T$ denotes the unnormalized Teplitz equation autocorrelation matrix. The recovery equation of the OS in MOMEDA is shown in Equation (11).

$$\vec{\boldsymbol{y}} = \boldsymbol{X}_0^T\vec{\boldsymbol{f}} \tag{11}$$

The investigation is simultaneously evaluated utilizing envelope demodulation following the noise reduction decomposition process of the FS by the enhanced CEEMD and the deconvolution of the RS after noise reduction by MOMEDA. Considering that not all IMF components generated by the

improved CEEMD decomposition belong to the valid ones, and spurious components can reduce the decomposition effect and thus affect the FD results. K, FIR, and PCC are thus used in the study as screening metrics for the IMF components in order to guarantee their validity. Of these, K is a measure of the particular peak state of a real random variable's probability distribution; Equation (12) provides the formula for its expression.

$$Ku = \frac{\mathrm{E}(x-\mu)^4}{\delta^4} \tag{12}$$

In Equation (12), E denotes the natural logarithm and x denotes the original VS of the bearing. Ku denotes the magnitude of the Kurtosis produced by the original VS, δ denotes the standard deviation (SD) of the original VS, and μ denotes the mean value of the original VS. The bearing is considered to be in acceptable condition when the K of the VS of the ABB is roughly equal to 3. The larger value of K of the IMF components at each stage obtained by CEEMD decomposition indicates that there is a larger amount of shock in the IMF signal of the corresponding order. The expression formula for FIR is given in Equation (13).

$$FIR = \frac{D(p_1)+D(p_2)+D(p_3)+D(p_4)+D(p_5)}{D_t} \tag{13}$$

In Equation (13), $p_1 \sim p_5$ denotes the 1-octave to 5-octave frequencies of the bearing fault, and $D(p_1) \sim D(p_5)$ denotes the amplitude of the 1-octave to 5-octave frequencies, respectively. D_t denotes the sum of the amplitudes of all points in the ES. PCC as a constant coefficient, which mainly reflects the same moving trend between two sets of linear data, the specific expression formula is shown in Equation (14).

$$Pcc_{\alpha,\beta} = \frac{Cov(\alpha,\beta)}{\sigma_\alpha \sigma_\beta} \tag{14}$$

In Equation (14), $Pcc_{\alpha,\beta}$ denotes the correlation coefficient between two variables that need to be analyzed for correlation. α and β denote the variables to be analyzed for correlation. σ_α and σ_β are the SD of the two variables. The PCC has a range of values from -1 to 1. A change in the same direction will result in a positive correlation, at which point the PCC is greater than 0 and vice versa. The absence of a linear connection between the two sets of data is indicated when PCC equals 0. Since K, FIR and PCC are all positively correlated to reflect the fault characteristics, and the difference between FIR and K or PCC is several orders of magnitude, the study chooses the product of the three as the Composite Indicators (KI) of FD, which is calculated as shown in Equation (15).

$$KI = Ku \times FIR \times Pcc \tag{15}$$

The IMF components at each stage generated by CEEMD decomposition are screened according to the KI value, and the diagnosis of the rolling stock ABB faults is realized by performing MOMEDA deconvolution based on the obtained RSs, and finally by performing the Hilbert envelope analysis [20]. Therefore, the specific flow of the proposed FD method (CEEMD-MOMEDA) for rolling stock ABB combining improved CEEMD and MOMEDA is shown in Fig. 3.

First, the imported ABB FSs are supplemented with a pair of GWN signals of the same magnitude and opposite direction. Next, CEEMDF decomposition is carried out to extract all the IMF components of each stage. The K, FIR, PCC, and KI values of the three are used to filter the IMF components. The IMF components with K greater than 3, PCC greater than 0.3, and larger FIR and KI are selected as diagnostic signals for reconstruction. Finally, the deconvolution calculation is performed using MOMEDA and the calculated signals are included for analysis.

4. EXPERIMENTAL VALIDATION OF A FAULT DIAGNOSIS METHOD FOR AXLEBOX BEARINGS IN MOVING TRAINS COMBINING IMPROVED CEEMD AND MOMEDA

The study employed the created ABB fault model for simulation analysis and signal modeling to confirm the effectiveness of the CEEMD-MOMEDA diagnostic technique. Second, experimental data validation was done using

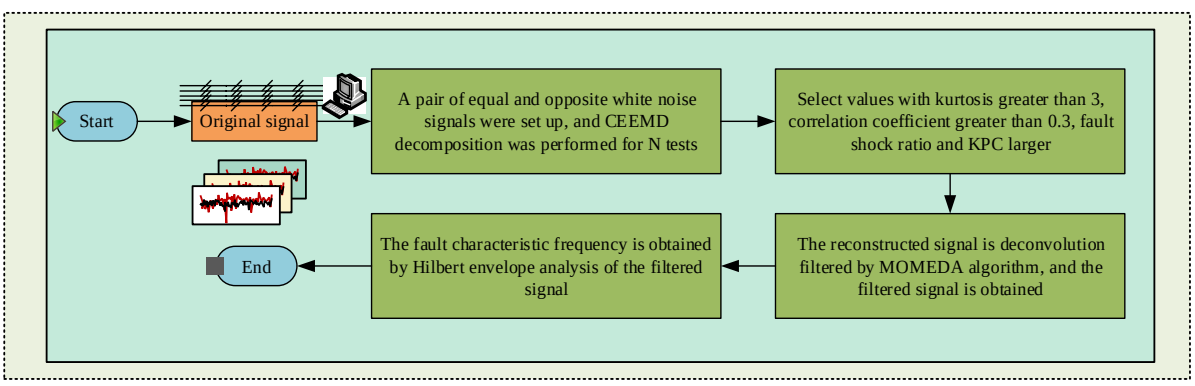

Fig. 3. CEEMD-MOMEDA processing flow

erroneous bearing data from the Case Western Reserve University (CWRU) Bearing Data Center.

4.1. Simulation data analysis

In order to realize effective simulation data verification, the study established an ABB fault model for signal simulation and set the relevant parameters. The test bench's resonance frequency is set to 2500 Hz, its fault impact count is 455, its impact attenuation coefficient is 400, and its beginning amplitude value is 1.15 m/s2. And the bearing rotational frequency is 214Hz, the impact time interval of adjacent faults is 8.33×103s, and the time error is about 1%-2% of the impact interval time of adjacent faults. According to the above parameters and the simulation signal at 12000Hz sampling frequency, 1.5s sampling time length is selected to generate a noise-free fault vibration model in MATLAB software, as shown in Fig. 4.

Fig. 4(a) displays the time domain waveform of the signal for the noise-free simulation. A noticeable periodic shock band is present in the graphic. The frequency domain plot of the signal for the noise-free simulation is shown in Fig. 4(b), and it is noticeable that the frequency domain's highest point is approximately 2500 Hz. In Fig. 4(c), the plot obtained after envelope demodulation analysis shows the transfer frequency (orange), the four inner-circle faults (red), and the corresponding transfer modulation frequency (blue) of the simulated signal (S-S). According to the time domain of this S-S, the study adds 18 levels of GWN to its signal and the two signals are superimposed into a mixed signal for CEEMD decomposition. The 6th order IMF components obtained from the CEEMD decomposition are shown in Fig. 5.

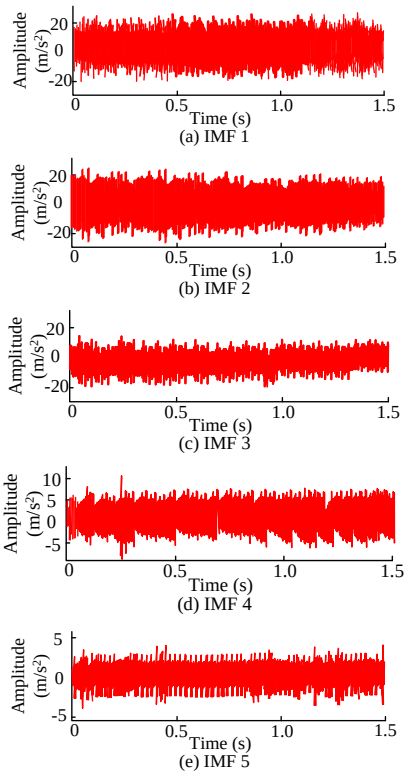

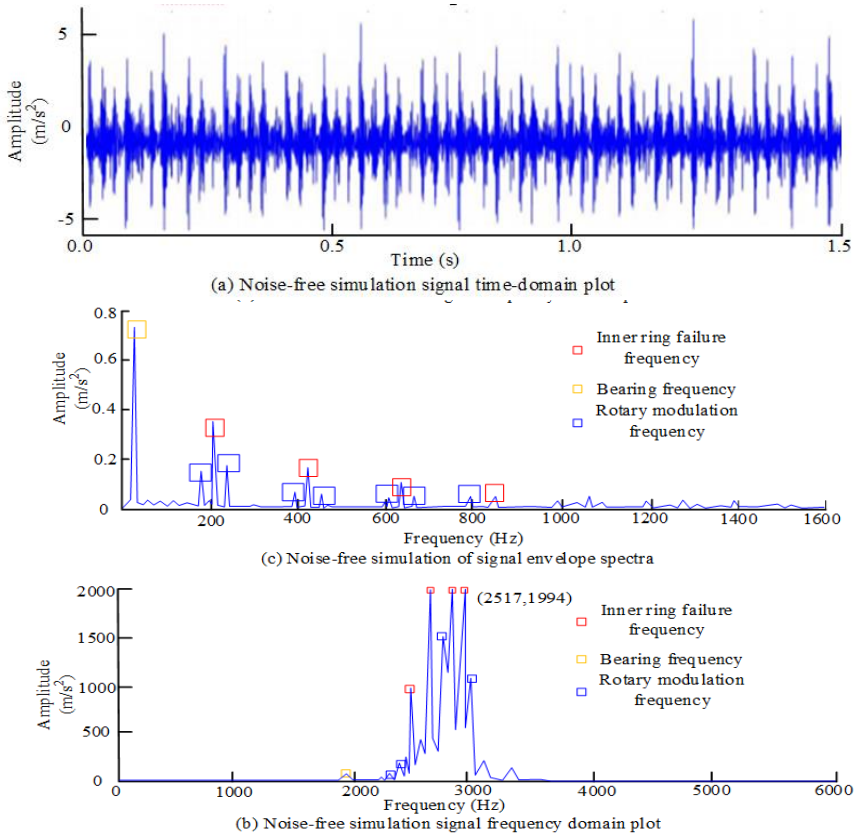

Fig. 4. Noise-free simulation of signal time domain, frequency spectrum and envelope spectra

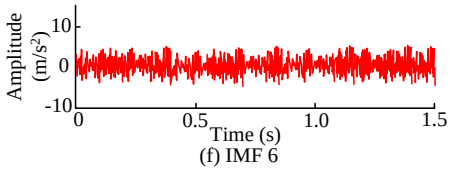

(f) IMF 6

Fig. 5. Plot of IMF components of each order after CEEMD decomposition

Figs. 5(a)-(f) displays the IMF component plots for the first six orders, respectively. It is evident that the signal amplitude of the IMF components acquired at each order varies slightly. The 6-order IMF components' corresponding K, FIR, PCC, and KI are computed, and the IMF components with K coefficients more than 3, PCC greater than 0.3, and larger FIR and KI are chosen for signal reconstruction. Table 1 displays the relevant indexes of the 6-order IMF components.

Table 1. The values of K, FIR, P CC, and KI corresponding to different IMFs

Index	IMF 1	IMF 2	IMF3	IMF4	IMF5	IMF 6
K	3.0863	2.2426	3.5913	2.9508	3.0647	2.8558
FIR	0.0018	0.0012	0.0028	0.0023	0.0012	0.0010
PCC	1	0.7661	0.4411	0.2871	0.2000	0.1879
KI	0.0056	0.0021	0.0044	0.0019	0.0007	0.0005

The three components in Table 1 have K values greater than 3, FIR values larger, PCC values greater than 0.3, and KI values largest amongst IMF1, IMF2, and IMF3; additionally, the three components have larger FIR values than IMF1, IMF3, and IMF4. Comprehensive comparison, the study selected IMF1 and IMF3 as the components of signal reconstruction. The specific results are shown in Fig. 6.

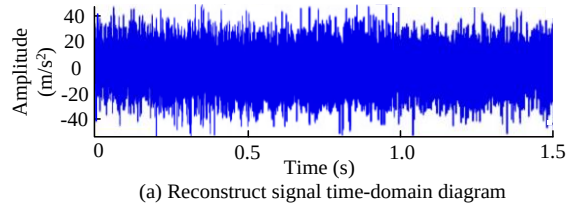

(a) Reconstruct signal time-domain diagram

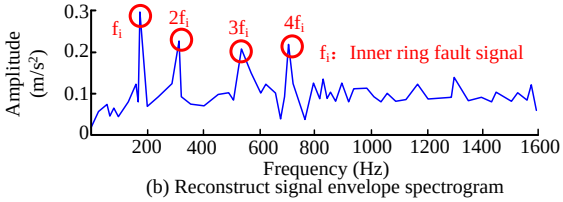

(b) Reconstruct signal envelope spectrogram

Fig. 6. The simulated signal reconstruction's envelope spectrum and time domain waveform

The RS's time-domain plot (TDP) and envelope spectrogram are shown in Figs. 6(a) and 6(b), respectively, throughout a 1.5-second period. The RS's frequency amplitude is increased by the FS, as the envelope spectrogram demonstrates. This suggests that the FS can be effectively deconstructed using CEEMD. A closer examination indicates that the envelope spectra of the RSs still contain additional interference frequencies. As a result, the research moves on to deconvolution in order to use MOMEDA to reconstruct the signal. Additionally, the signal spectra of the RSs following CEEMD deconvolution are compared with the signal spectra of the CEEMD deconvolution following MOMEDA, MED, and maximum correlation kurtosis deconvolution (MCKD) processing, respectively, to demonstrate the efficacy of the CEEMD-MOMEDA FD method suggested by the study. In MOMEDA processing, the window length (WL) of the finite pulse filter is set to 1500 with a period of 56.07, and the period interval of the deconvolution is taken to be [50,60]. In MED processing, its filter WL and iteration number are 30. In MCKD processing, the filter WL is 300, the iteration number is the same as that of MED, the displacement factor is 5, and the period is the same as that of MOMEDA. Fig. 7 displays the specific comparative results.

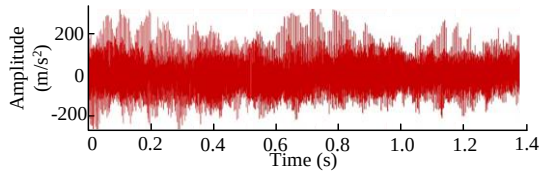

(a) Time domain diagram of reconstructed signal processed by MOMEDA

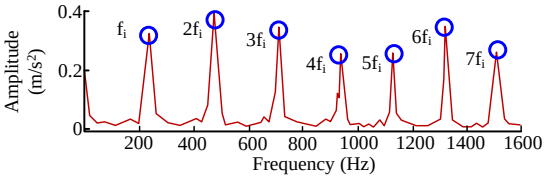

(b) The envelope spectrum of the reconstructed signal processed by MOMEDA

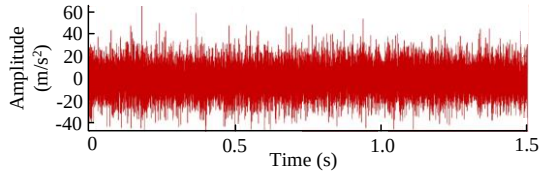

(c) Time domain diagram of reconstructed signal processed by MED

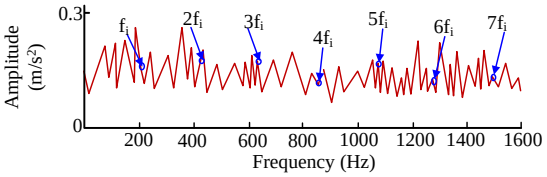

(d) The envelope spectrum of the reconstructed signal processed by MED

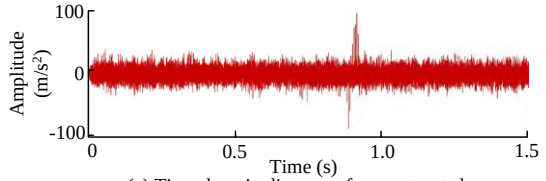

(e) Time domain diagram of reconstructed signal processed by MCKD

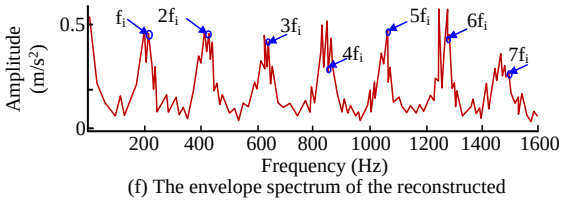

(f) The envelope spectrum of the reconstructed signal processed by MCKD

Fig. 7. Comparison of processing effects of three methods

Fig. 7(a) displays the TDP of the RS following MOMEDA processing. Fig. 7(c) displays the TDP following MDE processing; and Fig. 7(e) displays the TDP following MCKD processing. Following MOMEDA's processing of the RS, a comparatively strong periodic pulse component appears in the signal, indicating that the noise has been effectively reduced. The amplitude of the signal after MED processing is in the range of [-40,60], which indicates that its signal is not enhanced and the signal shock characteristics are not significant. And in the time-domain graph after MCKD processing, only the signal around 0.85s has been had strengthened, and the processing effect is the worst among the three methods. The comparison of the envelope spectra obtained from the three techniques of processing (Figs. 7(b), (d), and (f)) demonstrates that the bearing FS's distinctive frequency after MOMEDA processing is the most noticeable.

4.2. Experimental data Validation at CWRU

To further validate the reliability and reasonableness of the CEEMD-MOMEDA proposed by the study in the diagnosis of ABB FSs, the study was experimentally verified based on the faulty bearing data released by the Bearing Data Center of CWRU. The experimental motor bearing's outer ring (OR) has a diameter of 52 mm, while the inner ring's (IR) diameter is 25 mm. The characteristic frequencies of the OR and IR faults are 3.5848 and 5.4152, respectively. First, the IR fault data is used for the study. The bearing fault depth is determined by measuring the indentation of the electric spark, which is 0.1778 mm. The motor is configured to rotate at 1797 revolutions per minute, which is calculated to produce an IR fault of 162.19 hertz. Fig. 8 displays the outcomes of the initial envelope spectrogram and TDP.

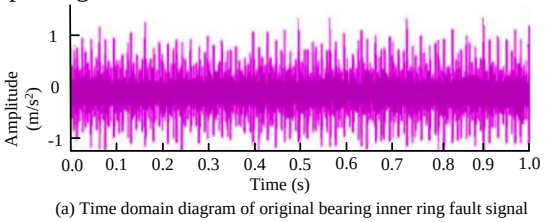

(a) Time domain diagram of original bearing inner ring fault signal

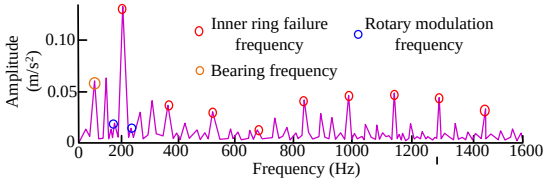

(b) Envelope spectrum of original bearing inner ring fault signal

Fig. 8. Envelope spectrum and time domain of the initial inner ring fault signal

The original FS time domain depiction of the bearing's IR in Fig. 8(a) makes the periodic influence of the signal very evident. The rotational frequency of the FS, which ranges from 1 to 9 times the frequency of the FS of the IR, is displayed in Fig. 8(b), along with the rotational modulation frequency around the 1 times frequency. To better diagnose the FS, the study added 6 levels of GWN for superimposed mixing in the inner circle FS. Simultaneously, the investigation contrasts the envelope and time-domain spectrograms of MCKD, MED, and the suggested postprocessing diagnostic approach. In MOMEDA processing, the WL of the finite pulse filter is set to 1500 and the period is 73.99, and the period interval of deconvolution is taken as [70,80]. Fig. 9 displays the specific comparative results.

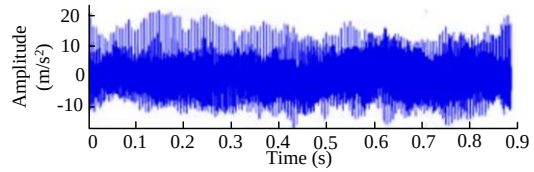

(a) Time-domain diagram of the bearing inner ring fault signal after MOMEDA processing

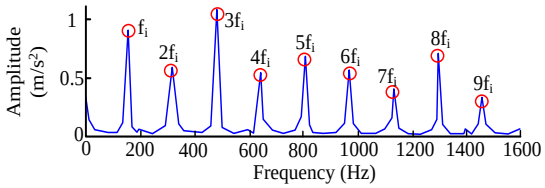

(b) Envelope spectrum of reconstructed signal of bearing inner ring fault after MOMEDA processing

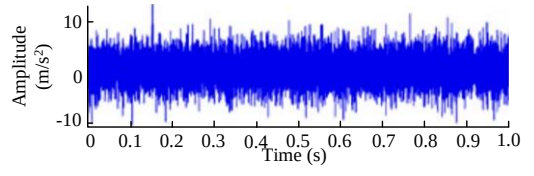

(c) Time-domain diagram of the bearing inner ring fault signal after MED processing

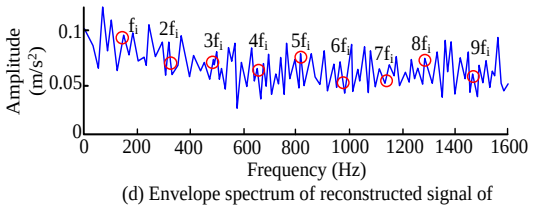

(d) Envelope spectrum of reconstructed signal of bearing inner ring fault after MED processing

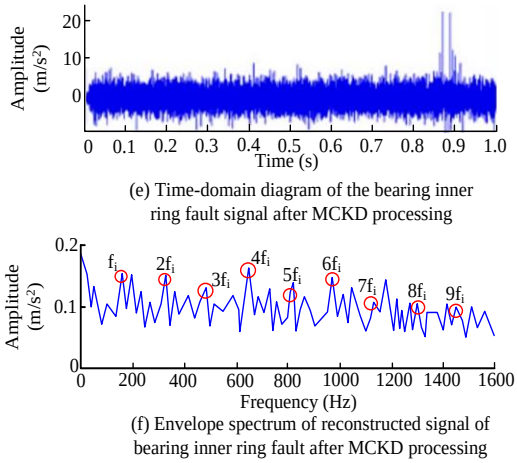

(e) Time-domain diagram of the bearing inner ring fault signal after MCKD processing

(f) Envelope spectrum of reconstructed signal of bearing inner ring fault after MCKD processing

Fig. 9. Comparison of the effect of the bearing inner ring fault signal after three methods of treatment

Figs. 9(a), 9(c), and 9(e) compare the TDPs of the FSs in the inner circle after processing by the three methods. The results indicate that MOMEDA has a stronger effect on noise processing than MED and MCKD, and that MCKD enhances the time-domain signals at approximately 0.9s, while MED does not. A comparison of the envelope spectra obtained from the three different methods of processing reveals that, in Fig. 9(b), the 1-9 times frequency can be seen after MOMEDA processing. In contrast, the characteristic and non-characteristic frequencies of the FS are mixed together in the MED and MCKD envelope spectra, making them difficult to distinguish. Simultaneously, the investigation conducted additional experimental validation of the bearing OR FS. Fig. 10 displays the envelope spectrogram and time domain map results of the OR's initial FS.

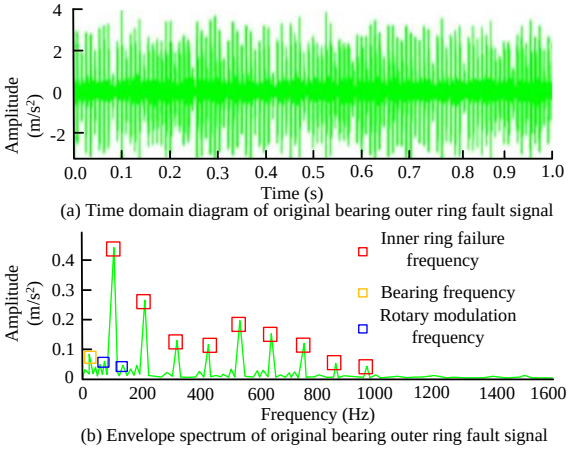

(a) Time domain diagram of original bearing outer ring fault signal

(b) Envelope spectrum of original bearing outer ring fault signal

Fig. 10. Time domain and envelope spectrum of the original bearing outer ring fault signal

It is evident from Figs. 10(a) and (b) that the OR bearing signal's TDP exhibits periodicity and a greater amplitude than the IR's. These spectra line up with the bearing's OR's initial FS. Consequently, the study added 14 levels of GWN to the OS. In MOMEDA processing, the WL of the finite impulse filter is set to 1500 and the period is 111.83, and the period interval for deconvolution is taken as [110,120]. The specific results are shown in Fig. 11.

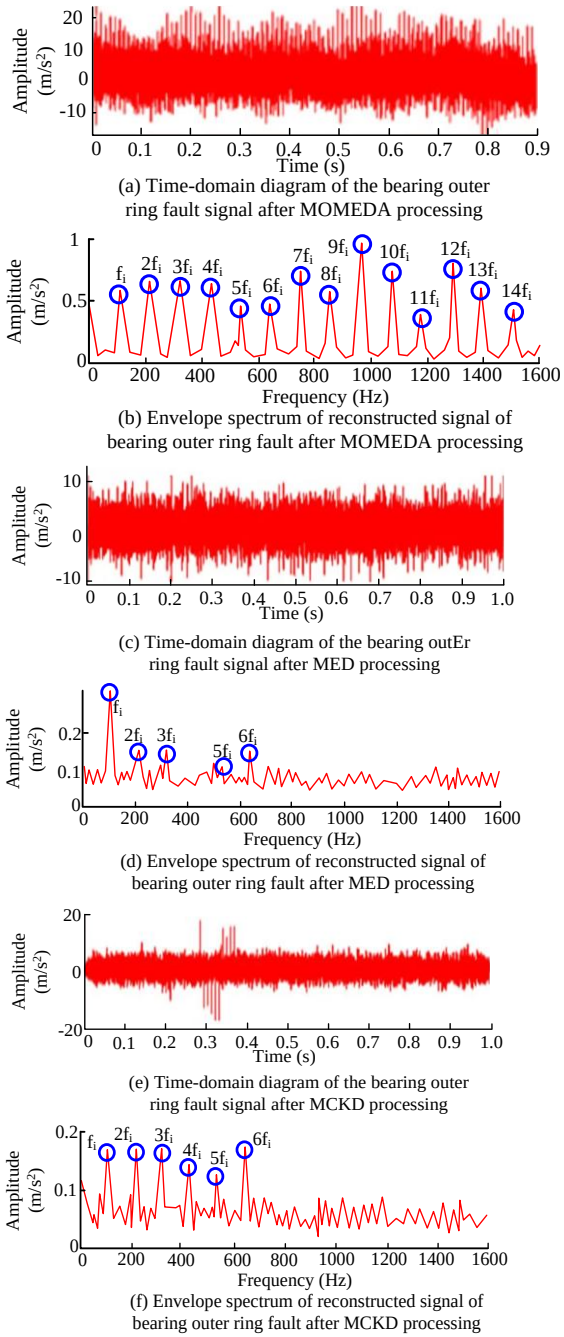

(a) Time-domain diagram of the bearing outer ring fault signal after MOMEDA processing

(b) Envelope spectrum of reconstructed signal of bearing outer ring fault after MOMEDA processing

(c) Time-domain diagram of the bearing outEr ring fault signal after MED processing

(d) Envelope spectrum of reconstructed signal of bearing outer ring fault after MED processing

(e) Time-domain diagram of the bearing outer ring fault signal after MCKD processing

(f) Envelope spectrum of reconstructed signal of bearing outer ring fault after MCKD processing

Fig. 11. Comparison of the effect of the bearing outer ring fault signal after three methods of treatment

The suggested diagnostic method's RSs of bearing OR faults are processed and displayed as TDPs and envelope spectra in Figs. 11(a) and (b). Comparing MED and MCKD, it can be noted that all the amplitudes of the TDPs after MOMEDA processing are enhanced, and the 1-14 times eigen frequency of the FS can be visualized. The aforementioned findings demonstrate the excellent applicability of the CEEMD-MOMEDA diagnostic approach in the CWRU bearing fault dataset, as well

as the good logic and reliability of MOMEDA's deconvolution of RSs.

5. CONCLUSION

Aiming at the influence of interference or noise generated by the external environment of the ABB test bed of rolling stock in VM as well as simulation methods, the study proposes a FS diagnosis method by combining the improved CEEMD and MOMEDA. Verification by simulation experiment indicated that the CEEMD can decompose the bearing FS efficiently and that the screened IMF component's FS eigen frequency is more observable and consistent. When RSs are processed using MOMEDA, the FS's time-domain amplitude may be efficiently increased. Additionally, analyzing the envelope spectra of the RS processing is easier with MOMEDA than with MED and MCKD. CWRU dataset validation revealed that the research-proposed methodology enables effective diagnosis in both inner and OR FSs. When compared to alternative techniques, the OR's fault characteristic frequency was 1-14 octaves, and the envelope spectrogram of the FS of the IR of CEEMD-MOMEDA showed a frequency of 1-9 octaves. The study's CEEMD-MOMEDA diagnostic method, whose calculation is more straightforward and efficient, demonstrated an effective ability to identify both outer and IR problems in ABB. IMF component screening using Kurtosis, correlation coefficient and other metrics can enhance the identification and diagnostic effect of FSs. However, the study still has certain shortcomings. The bearing vibration model established by the study saves in a certain idealization and mainly adopts the form of wear for bearing failure simulation. To realize the high efficiency of BFD for rolling stock, the study will carry out additional experimental tests in additional bearing fault scenarios using the suggested diagnostic approach in the future.

Source of funding: *The research is supported by: Higher Education Science and Technology Research Project of Hebei Province (Project No: ZC2023048).*

Author contributions: *research concept and design, J.S.; Collection and/or assembly of data, (Y.Z.; Data analysis and interpretation, Y.L.; Writing the article, J. S.; Critical revision of the article, Y.L.; Final approval of the article, Y.Z..*

Declaration of competing interest: *The authors declare that they have no known competing financial interests or personal relationships that could have appeared to influence the work reported in this paper.*

REFERENCES

1. Wang J, Yang J, Bai Y, Zhao Y, He Y, Yao D. A comparative study of the vibration characteristics of railway vehicle axlebox bearings with inner/outer race faults. Proceedings of the Institution of Mechanical Engineers, Part F: Journal of Rail and Rapid Transit 2021; 235(8): 1035-1047.
2. Bandewad G, Datta KP, Gawali BW, Pawar SN. Review on discrimination of hazardous gases by smart sensing technology. Artificial Intelligence and Applications 2023; 1(2): 86-97.
3. Wu X, Gao A, Wen Z, Wu S, He S, Chi M, et al. Online estimation of fatigue damage of railway bogie frame based on axle box accelerations. Vehicle System Dynamics 2023; 61: 286–308. https://doi.org/10.1080/00423114.2022.2041204.
4. Yi C, Huo H, Liao X, Zhou L, Ran L, Lin J. Investigation on the characterisation of axle box resonance characteristics to wheel excitation. Vehicle System Dynamics 2023; 61(9)
5. Martynov I, Gerlici J, Trufanova A, Petuhov V, Shovkun V, Kravchenko K. Development of a Procedure for Determining the Pre-Failure Condition of the Axle Boxes of Railway Rolling Stock. Communications - Scientific letters of the University of Zilina 2022; 24: B87–93. https://doi.org/10.26552/com.C.2022.1.B87-B93.
6. Gao P, Yu T, Zhang Y, Wang J, Zhai J. Vibration analysis and control technologies of hydraulic pipeline system in aircraft: A review. Chinese Journal of Aeronautics 2021; 34(4): 83–114. https://doi.org/10.1016/j.cja.2020.07.007.
7. Aviña Corral V, Rangel-Magdaleno J, Morales-Perez C, Hernandez J. Bearing Fault detection in ASD-powered Induction Machine by using MCSA and Goodness-of-Fit Tests. IEEE Transactions on Industrial Informatics 2021; 1–1. https://doi.org/10.1109/TII.2021.3061555.
8. Zhou P, He L, Yi C, Lin J, He L, Hu Q. Impulses recovery technique based on high oscillation region detection and shifted rank-1 reconstruction - Its application to bearing fault detection. IEEE Sensors Journal; 22(8): 8084–93. https://doi.org/10.1109/JSEN.2022.3159116.
9. Habbouche H, Amirat Y, Benkedjouh T, Benbouzid M. Bearing Fault Event-Triggered Diagnosis Using a Variational Mode Decomposition-Based Machine Learning Approach. IEEE Transactions on Energy Conversion 2022; 37: 466–74. https://doi.org/10.1109/TEC.2021.3085909.
10. Zhou Q, Zhang Y, yi C, Lin J, He L, Hu Q. Convolutional sparse coding using pathfinder algorithm-optimized orthogonal matching pursuit with asymmetric gaussian chirplet model in bearing Fault Detection. IEEE Sensors Journal 2021; 1–1. https://doi.org/10.1109/JSEN.2021.3086015.
11. Hosseinpour Zarnaq M, Omid M, Aghdam E. Fault diagnosis of tractor auxiliary gearbox using vibration analysis and random forest classifier. Information Processing in Agriculture2021; https://doi.org/10.1016/j.inpa.2021.01.002.
12. Wang Y, Yang M, Li Y, Xu Z, Wanga J, Fang X. A Multi-input and multi-task convolutional neural network for fault diagnosis based on bearing vibration signal. IEEE Sensors Journal 2021; 1–1. https://doi.org/10.1109/JSEN.2021.3061595.
13. Zhang Q. Relay vibration protection simulation experimental platform based on signal reconstruction of MATLAB software. Nonlinear Engineering 2021; 10(1): 461–8. https://doi.org/10.1515/nleng-2021-0037.
14. Li G, Zheng C, Yang H. Carbon price combination prediction model based on improved variational mode

decomposition. Energy Reports 2022; 8: 1644–64. https://doi.org/10.1016/j.egyr.2021.11.270.
15. Karan B, Sekhar Sahu S. An improved framework for Parkinson's disease prediction using Variational Mode Decomposition-Hilbert spectrum of speech signal. Biocybernetics and Biomedical Engineering 2021; 41(2). https://doi.org/10.1016/j.bbe.2021.04.014.
16. Dou H, Liu Y, Chen S, Zhao H, Bilal H. A hybrid CEEMD-GMM scheme for enhancing the detection of traffic flow on highways. Soft Computing 2023; 27: 1–16. https://doi.org/10.1007/s00500-023-09164-y.
17. Zhang X, Wu X, He S, Zhao D. Precipitation forecast based on CEEMD–LSTM coupled model. Water Supply 2021; 21(8): 4641–57. https://doi.org/10.2166/ws.2021.237.
18. Xie X, Yang Z, Zhang L, Zeng G, Wang X, Zhang P, et al. An improved Autogram and MOMEDA method to detect weak compound fault in rolling bearings. Mathematical Biosciences and Engineering 2022; 19(10): 10424–44. https://doi.org/10.3934/mbe.2022488.
19. Xiong Y, Yan Z, Huang K, Chen H. Research on gear fault diagnosis method based on SSA–VME–MOMEDA. Transactions of the Canadian Society for Mechanical Engineering 2023; 47(2): 185–201. https://doi.org/10.1139/tcsme-2022-0093.
20. Kabul A, Ünsal A. Detection of broken rotor bars of induction motors based on the combination of Hilbert envelope analysis and Shannon entropy. tm - Technisches Messen 2021; 88(1): 45–58. https://doi.org/10.1515/teme-2020-0066.

Jiuli SHEN
Born in Suihua City, Heilongjiang Province in 1982. He obtained a bachelor's degree in Measurement and Control Technology from Yanshan University in 2007, a master's degree in Instrumentation Engineering from Yanshan University in 2013, and a doctoral degree in Control Science and Engineering from Yanshan University in 2023. He has been teaching at Huzhou Vocational and Technical College since 2023. His main research interests are the fault diagnosis of rolling bearings and infrared detection, etc. Now he has published more than 10 academic papers and 3 patents.
e-mail: sjlysu2016@sina.com

Yan ZENG
Born in Xingtai City, HeBei Province in 1987. She received bachelor degree from Lanzhou University of Technology in 2011 and master degree from Northwestern Polytechnical University in 2014. She is a lecturer in Tangshan Polytechnical University since 2014. Her research interests are digital image processing, compressed sensing, etc. Now she has published more than 20 academic papers and 5 patents.
e-mail: zengyan3925@163.com

Yikao LIU
Born in Jining City, Shandong Province in 1986. He Obtained a Bachelor's degree from Shandong Jiaotong University in 2017.He has been teaching at Huzhou Vocational and Technical College since 2023.His main research interests include mechanical design, CNC machining technology, and intelligent detection technology. He has now published 6 academic papers, including 2 in Peking University core journals and 6 patents.
e-mail: 405726090@qq.com